INSIGHTS INTO DIAGENESIS AND PORE STRUCTURE OF OPALINUS SHALE THROUGH COMPARATIVE STUDIES OF NATURAL AND RECONSTITUTED MATERIALS

Ali Seiphoori[1],*, Andrew J. Whittle[1], Konrad J. Krakowiak[2], and Herbert H. Einstein[1]

[1] Department of Civil and Environmental Engineering, Massachusetts Institute of Technology (MIT), Cambridge, MA 02139, USA
[2] Department of Civil and Environmental Engineering, University of Houston, Houston, TX 77204, USA

Abstract—Shales have undergone a complex burial diagenesis that involved a severe modification of the pore structure. Reconstituted shales can provide new insights into the nature of the pore structure in natural materials. The effects of diagenesis on the microfabric, pore size distribution, and porosity of Opalinus shale were measured by comparing the behavior of natural and reconstituted specimens. The parent material (Opalinus shale) was reconstituted through multiple grinding operations, sedimentation from a dispersed slurry, and one-dimensional isothermal consolidation. This process produced uniform specimens that were not cemented and had replicable microfabric and engineering properties. The microfabric and mineralogy of the materials were examined using high-resolution scanning/backscattered electron microscopy (SEM/BSEM) and energy-dispersive X-ray spectroscopy (EDS) for specimens with broken and milled surfaces. Mercury intrusion porosimetry (MIP) and N_2 adsorption were used to assess the pore size distributions and specific surface areas of the materials. The microstructure of natural shale was characterized to be highly heterogeneous with significant concentrations of calcareous microfossils, calcite, and quartz particles embedded within the clay matrix. The microfossils were observed to be locally infilled and rimmed by a calcite cement that showed evidence of dissolution. The reconstituted specimens showed a double-structure microfabric that evolved with the level of consolidation stress and converged into a single-structure material (comparable to the natural shale) at a consolidation stress of more than twice the estimated maximum *in situ* effective stress. The natural shale had a lower specific surface area in comparison to the reconstituted material, which was consolidated at large effective stresses. These differences can be attributed to cementation at a submicron pore scale and highlight chemical diagenesis effects that were not replicated in the reconstituted specimens.

Key Words—Burial Diagenesis, Mercury Intrusion Porosimetry (MIP), Microfossils, Nitrogen Gas Adsorption, Reconstituted Specimens, Scanning/Backscattered Electron Microscopy(SEM/BSEM).

INTRODUCTION

Understanding the microfabric and pore structural properties of shales is critical in quantifying the performance of these materials for a wide range of applications. Shales have been chosen as caprocks in geological systems for carbon sequestration (Rutqvist, 2012). Shales are also under consideration as the host rocks in geological repositories for high-level radioactive waste (Marschall *et al.*, 2005). To evaluate the sealing capacity of shales in such applications, the pore structure and mass transport properties of shale need to be evaluated in detail. Organic-rich shales are important sources of natural gas and oil and the production of shale gas and oil requires a detailed knowledge of the porosity and permeability (*e.g.*, Ambrose *et al.*, 2012) as well as the mechanical properties (Ortega *et al.*, 2011). The pore structure of shale evolved during the course of sediment consolidation due to an increase in the effective vertical

pressure and other diagenetic processes, such as the precipitation of mineral cements from the pore fluid and phase transformations of clay and non-clay minerals (Parker, 1997). Pressure dissolution can occur at grain contacts subjected to stress gradients (Sheldon *et al.*, 2003), while dissolved components can be either removed from or deposited within the pore space. Large contact stresses between particles can result in a change in the size or shape of mineral crystals (*i.e.*, recrystallization), where strong molecular bonds can be formed due to physical interactions at the contact surfaces. Precipitation results in the formation of cementing agents, such as quartz, feldspar, and carbonate minerals, which can lithify the sediments and bind the components together. Along with the pore water composition, temperature change is likely the key factor in the dissolution and precipitation of clay minerals because it can make some of the minerals unstable (Dræge *et al.*, 2006). The transformation of smectite into illite and quartz can occur at $60-80^{\circ}C$. Additionally, an ion-rich smectite can be dissolved and precipitated as chlorite, and Mg-rich smectite can be replaced by corrensite (Bjørlykke and Aagaard, 1992). The clay

and non-clay phase transformations associated with diagenesis have been well studied (*e.g.*, Tourtelot, 1979; Curtis, 1980; Scotchman, 1989; Awwiller, 1993; Gaupp *et al.*, 1993; Hillier, 1993; Huggett, 1993; Cruz and Reyes, 1998). High resolution backscattered and scanning electron microscopy have been used to investigate diagenetic dissolution and alterations in sedimentary formations (Shaw and Primmer, 1991; Kim *et al.*, 1998; Desbois *et al.*, 2011, 2014; Slatt and O'Brien, 2011; Houben *et al.*, 2013, 2014; Laurich *et al.*, 2017). Despite the importance of pore structure modifications due to consolidation and the impact of diagenetic cementation, few studies have systematically investigated the evolution of pore structures in argillaceous formations (*e.g.*, Nygård *et al.*, 2004; Chalmers and Bustin, 2015). Within the geotechnical community, reconstituted soils are frequently used to investigate 'intrinsic' properties (*e.g.*, Burland, 1990) as a basis for understanding the behavior of natural *in situ* 'structured' materials (*e.g.* Leroueil and Vaughan, 1990; Cotecchia and Chandler, 1997; Abdulhadi *et al.*, 2010; Chandler, 2010; Schneider *et al.*, 2011; Hong *et al.*, 2012; Adams *et al.*, 2013). A few studies have investigated the behavior of natural argillaceous formations by testing reconstituted specimens. William and Airey (2009) compared the compressive behavior of reconstituted and natural Bringelly shale samples at the same density and reported a relatively minor influence of diagenesis that was revealed as very slight cementation. In contrast, Nygård *et al.* (2004) reported a significant effect of diagenesis on the mechanical and transport behavior of Kimmeridge shale, which implied that mechanical compaction alone cannot produce the much lower porosity, compressibility, and permeability of natural shales in comparison to the reconstituted materials. Favero *et al.* (2016) recently compared the 1-D oedometric behavior of reconstituted and intact Opalinus shale specimens from two different sites and depths. They measured a higher stiffness and lower porosity for the natural Opalinus shale and attributed the stiffness and porosity differences to chemical diagenetic processes. The purpose of the present study was to investigate the effects of diagenetic cementation on the pore structure of natural argillaceous formations through comparisons between natural and reconstituted specimens of Opalinus shale. Reconstituted specimens were prepared by developing a technique to disintegrate cementation in the natural material through multiple grinding processes. The powdered shale was then mixed with water in a sediment slurry and was incrementally consolidated to a target value of effective axial pressure. This procedure generated homogenized specimens with repeatable physical characteristics and engineering properties and enabled a detailed investigation of how the pore structure (porosity and pore size distribution) evolves with consolidation pressure.

MATERIAL AND METHODS

Opalinus Shale

Opalinus clay shale was obtained from the Full-scale Experiment (FE) tunnel of the Mont Terri Underground Research Laboratory (URL). The URL is located in the Jura Mountains of NW Switzerland at a depth of approximately 250 to 300 m. The FE tunnel is located in the clay-rich facies of the Opalinus shale formation (Freivogel and Huggenberger, 2003). The Mont Terri Opalinus shale was deposited during the Aalenian stage of the Middle Jurassic and was subjected to two successive burial stages in the Cretaceous and Tertiary with a maximum burial depth of about 1,350 m during the Cretaceous and 1,000 m during the Miocene (Mazurek *et al.*, 2006). Tectonic events during Alpine orogeny resulted in tilting and uplift of the claystone strata, and the combination of pre-loading by glaciers and erosion caused the current state of over consolidation (Bock, 2000). Specimens of the Mont Terri Opalinus shale exhibited intense slaking behavior when immersed in distilled water, which suggests very slight cementation in the natural state. Reconstituted shale specimens were prepared from powdered shale obtained through multiple grinding operations that reduced the intact parent material into a dry powder with more than 99% by weight <150 μm (see Seiphoori *et al.*, 2016). The particle size distribution of the powdered shale was measured using particle dispersion and sedimentation analysis with an ASTM 152H hydrometer (Figure 1a). The shale powder contained 30% <2 μm clay and 10% >60 μm sand. The mineral phases were mapped on a photomicrograph of the pulverized shale using an energy dispersive X-ray spectroscopy (EDS) analyzer to highlight the effectiveness of the grinding process in disintegrating the constituent particles of the natural material (Figure 1b). The basic physical and geotechnical index characteristics of the Opalinus shale are summarized in Table 1. The specific gravity was measured using the ASTM D854 method, while the average porosity ($n = 0.17$; void ratio $e = 0.20$) was measured using a liquid displacement technique with a non-polar liquid (Péron *et al.*, 2006; Seiphoori, 2014). The Atterberg limits were also measured using the ASTM D4318 method (Table 1). The pulverized shale can be classified as a low plasticity clay because a small effective surface area affects interactions of the clay with water. The soil activity (A) is defined as the ratio of the plasticity index (PI = $w_l - w_p$) to the percent clay (A = PI /% clay, after Skempton, 1953). The pulverized shale soil activity (A) was about 0.53, which is in the illite activity range (Das, 2008). The bulk mineralogy was identified using X-ray powder diffraction (XRPD) analysis (Table 2). Prior to the XRPD tests, the whole shale specimens were wet ground (in ethanol) and then spray dried to produce a random powder. Quantitative analysis was done using a normalized full-pattern
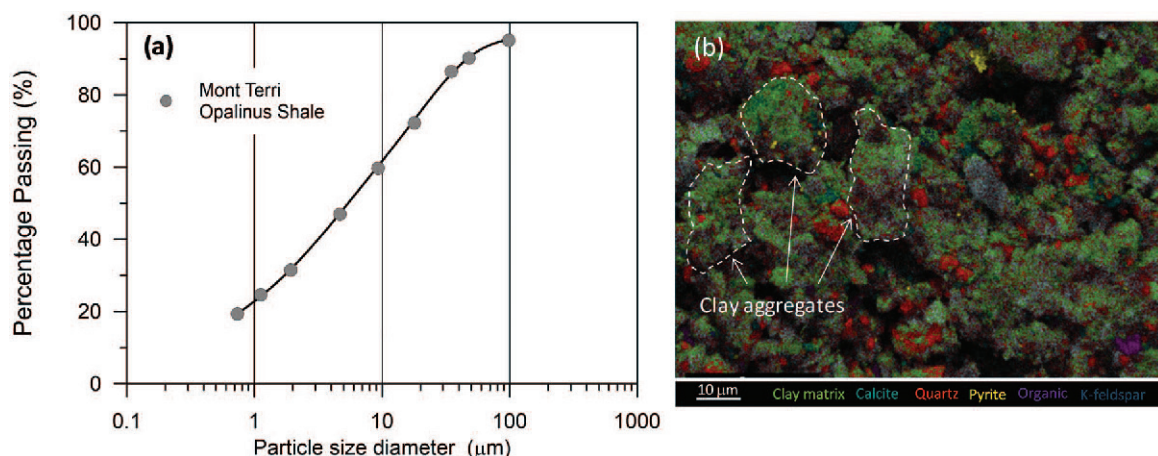
Figure 1. Grain-size distribution (a) of the Mont Terri Opalinus shale, (b) mineral phase map of the ground shale showing disintegration and breakage of particles and clay aggregates.

reference intensity ratio (RIR) method (*e.g.* Snyder, 1992). Clay minerals, including illite (I), illite−smectite mixed layer (I−S), kaolinite, and chlorite, comprise 65.7% of the Opalinus shale. The content of I−S mixed layer minerals accounts for 81% by weight of the clay fraction. Opalinus shale can be classified as a claystone based on the soil activity (Table 1), the mineralogy (Table 2), and a siltstone based on the particle size distribution (Figure 1a).

Reconstituted specimen preparation

The dry, ground shale powder was mixed to 80% water content to create a stable, workable slurry that had minimal particle segregation during consolidation. In general, the amount of water required for a consistent slurry varies depending on the material plasticity and salinity. The water content to use in the slurry was selected from trials with $w/w_l = 0.75-2.0$, where w is the gravimetric water content and w_l is the liquid limit in Table 1 according to prior studies (*e.g.*, Skempton and Jones, 1944; Burland, 1990; Allman and Atkinson, 1992; Cotecchia and Chandler, 1997; Abdulhadi *et al.*, 2010; Schneider *et al.*, 2011; Adams *et al.*, 2013; Seiphoori *et al.*, 2016). The slurry was prepared by first mixing the shale powder with distilled water and degassing the solution using vacuum (40−60 cm Hg) for 20−30 min to remove any trapped air bubbles. The slurry was then poured into rigid-walled sedimentation columns ('consolidometer') shown schematically in Figure 2.

Prior to slurry placement, the internal surface of the consolidometer column was coated with a thin layer of silicone oil to reduce the peripheral friction during the consolidation process. The base of each consolidometer was plugged with a porous disc and filter paper that rested on a PVC spacer. The consolidometer column was set up inside a reservoir filled with water to allow drainage from the bottom. Once the slurry was poured into the column, a filter paper and porous disc were placed on the top of the slurry. The system allowed drainage from the top by keeping a constant water level above the upper porous disc. This configuration ensured drainage from both ends of the consolidometer column. The slurry was then consolidated (under one-dimensional loading with zero lateral strain, *i.e.*, K_0 conditions) over time until a target axial effective stress (σ'_v) was reached through a series of incremental loads (j) specified by a load increment ratio, LIR = $(\sigma'_v[j+1]/\sigma'_v[j] - 1)$ ~1 (see Notation section for the definition of symbols). Once the maximum stress was reached, the specimen was unloaded to an over-consolidation ratio, OCR = $\sigma'_p/\sigma'_v = 4$ (where σ'_p is the maximum vertical effective stress), that corresponded to an isotropic effective stress condition (K_0 ~1.0; Germaine, 1982; Adams *et al.*, 2013). The specimen was then extruded using a hydraulic jack without changing the material stress state or porosity. The reconstituted materials were cut into small specimens suitable for microstructural observations and porosimetry analyses, which are detailed in the next sections.

Table 1. Physical and index characteristics of Opalinus shale (OPA).

Parameter	Depth (m)	G_s	ρ_d* (g/cm^3)	n	w_l (%)	w_p (%)	A**
OPA-shale	~300	2.75	2.29	0.17	37.6	21.8	0.53

* ρ_d is the dry density of the shale measured after dehydrating the material at 105ºC for 24 h
** A is the soil activity defined as $(w_l - w_p)/(\% <2~\mu m$ by weight), after Skempton (1953).

Table 2. XRPD bulk mineralogy of Mont Terri shale approximately by percent weight (modified from Morgan, 2015).

Quartz	13	Muscovite	2
Calcite	13		
Dolomite	<2	Trioctahedral chlorite	3
K-feldspar, plagioclase	<2	Kaolinite	18
Siderite, pyrite	<2	Illite+Illite-Smectite	44
Apatite, anatase	<2	Mixed layers	

High Resolution Scanning and Backscattered Electron Microscopy

Electron microscopic observations were carried out on both natural and reconstituted shale specimens using a Carl Zeiss Merlin HR-SEM system (ZEISS AG, Jena, Germany) that was equipped with an electron backscatter diffraction (EBSD) analyzer, which also provided energy-dispersive X-ray spectroscopy (EDS) for chemical phase analysis. Electron microscopy imaging in both scanning and backscattered modes and EDS analyses were carried out at 15 kV at a working distance of 10 mm. Observations were carried out on both broken surfaces and broad ion beam (BIB) milled surfaces of the material. Smooth, 2D surfaces of Opalinus shale were prepared using a JEOL SM Ar-ion cross section polishing system (JEOL Ltd., Tokyo, Japan) with an accelerating voltage of 6 kV, a sample current of

Figure 2. A schematic illustration of the consolidometer used to consolidate the sediment slurries.

2.8 mA, and a milling time of 8−10 h. The natural shale specimens were cross-sectioned perpendicular to the plane of fissility and the reconstituted specimens were cross-sectioned parallel to the consolidation direction. Both natural and reconstituted specimen series were mounted to SEM stubs using carbon tape and were coated with a 10 nm carbon layer to provide a conductive surface.

Porosimetry analysis

Mercury intrusion porosimetry (MIP). Mercury intrusion porosimetry (MIP; Washburn, 1921) has been widely used for investigating the microfabric and pore structure of various porous media that include shales and compacted clays previously subjected to different hydraulic and mechanical stress paths (*e.g.* Howard, 1991; Ninjgarav *et al.*, 2007; Romero and Simms, 2008; Loucks *et al.*, 2009; Koliji *et al.*, 2010; Clarkson *et al.*, 2012; Kuila and Prasad, 2013; Sasanian and Newson, 2013; Seiphoori *et al.*, 2014; Yu *et al.*, 2016). In the present study, the pore structure of reconstituted specimens was investigated at different consolidation stress levels using MIP. For idealized cylindrically shaped pores, the equivalent pore entrance diameter, d, is inversely proportional to the applied mercury pressure:

$$p_{Hg} = \frac{4\gamma_{Hg}\cos\theta}{d} \quad (1)$$

where γ_{Hg} is the surface tension of mercury (Hg) in vacuum and θ is the contact angle between Hg and the soil particles. Following Diamond (1970), the current analyses assume that γ_{Hg} = 0.485 N/m and θ = 147º, which is an average value obtained for kaolinite and illite; however, a lower average value of θ = 139º was reported for smectites. The MIP tests were carried out using an AutoPore IV (Micromeritics Instrument Corp., Norcross, Georgia, USA) Hg intrusion porosimeter device that attains a maximum intrusion pressure of 230 MPa, which corresponds to a pore entrance diameter of approximately 7 nm from equation 1. The results were presented in terms of the cumulative void ratio and the pore size density function (PSD = $-\Delta e_{HG}/\Delta[\log d]$), which were plotted against the pore entrance diameter (d), where e_{HG} is the equivalent void ratio computed from the intruded Hg volume of the specimens. The
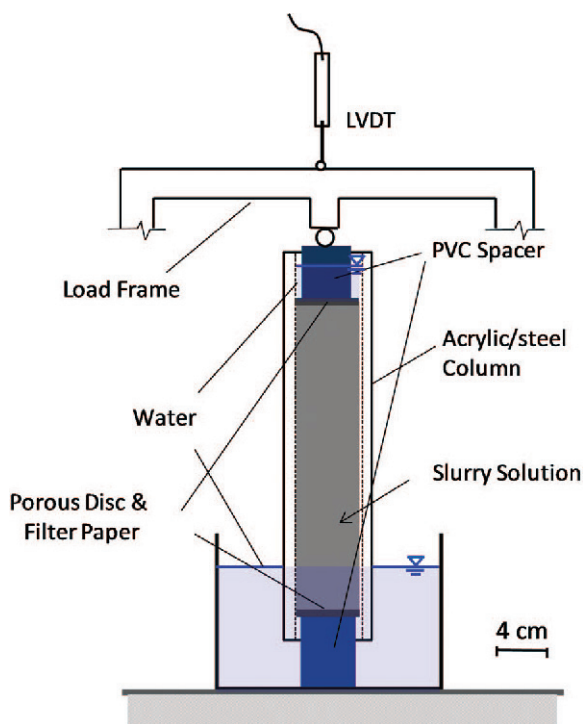
intrusion measurements are controlled by the pore throat diameters (Dullien, 1975; Larson and Morrow, 1981; Howard, 1991) and, thus, absolute pore sizes are not measured by the MIP technique. The measured MIP information, however, characterizes the relative dimensions of the pore space and the distribution within the porous structure of the material.

Nitrogen gas-adsorption technique. Nitrogen adsorption is often used to characterize the pore structure and the specific surface area of microporous media, such as shales for pore diameters in the range of $d = 2-200$ nm (*e.g.* Kuila and Prasad, 2013). While the MIP intrusion measurements are influenced by pore throat/entrance diameters (equation 1), N_2 gas adsorption is controlled by the pore body because it is governed by the capillary condensation mechanism. The volume of adsorbed gas on the specimen surface was measured for a relative equilibrium adsorption pressure (p/p_0) at the given temperature and pressure, where p is the absolute equilibrium pressure and p_0 is the N_2 condensation pressure. The pressure was progressively increased up to the condensation pressure p_0 (adsorption branch) followed by a reduction of N_2 pressure from p_0 (desorption branch). The gas adsorption isotherm was presented in terms of the volume of gas adsorbed with respect to p/p_0. Kuila and Prasad (2013) explained the different mechanisms that control the adsorption of N_2 in a porous medium under different applied relative pressures (p/p_0). At relative pressures above 0.4 p/p_0, N_2 condenses as a liquid phase in the pores due to capillary condensation. The pore size distribution is generally derived from the absorption isotherm using the computational procedure presented by Barrett *et al.* (1951), while the specific surface area of the particles is obtained from BET (Brunauer, Emmett, and Teller) theory to determine the amount of N_2 (in moles) required to cover the total surface area of the material, which is referred to as the statistical 'monolayer' (Brunauer *et al.*1938). The specific pore volume can be calculated by the liquid molar volume of the adsorbed N_2 at a relative pressure, $p/p_0 = 0.99$, which corresponds to a pore diameter of $d = 193.5$ nm (Gregg and Sing, 1983). To estimate the pore volume of the specimens in this study, the technique proposed by Harkins-Jura (Webb and Orr 1997) was used. The N_2 adsorption experiments were carried out using a Micromeritics 3Flex surface area analyzer (Micromeritics Instrument Corp., Norcross, Georgia, USA). The specimens were degassed at 105ºC for at least 24 h under a vacuum of 10 μm Hg. Prior to the tests, the shale specimens were crushed and passed through a #40 sieve (opening size of 420 μm) to decrease the equilibrium time for N_2 to reach the internal pore structure of the material as suggested by Kuila and Prasad (2013). Although a direct comparison of the pore volumes obtained from these two techniques is not recommended, a combination of MIP and N_2 gas

adsorption makes it possible to characterize the pore structure of complex porous media, such as shales over a wide range of pore sizes (*e.g.*, Gregg and Sing, 1983; Kuila and Prasad, 2013).

Specimen preparation for microstructural analysis. Both electron microscopy and porosimetry analyses (MIP and N_2 adsorption) require dry specimens. Careful attention needs to be given to this aspect of specimen preparation because reconstituted specimens at higher water contents can undergo shrinkage upon drying. The specimen volume will decrease during dehydration under different preparation techniques that include freeze drying, acetone drying, and air drying as well as oven drying (Thompson *et al.*, 1985; Simms and Yanful, 2002; Sasanian and Newson, 2013; Burton *et al.*, 2015). The variation in the void ratios (and porosity) of reconstituted shales versus the applied consolidation stress was calculated from the water content data (Figure 3). The water contents and porosity data were obtained after saturated specimens were extruded from the consolidometer and the water contents were measured (See Table 3). The MIP porosity data were obtained by using the MIP technique to measure the total volume of the dehydrated material (See equation 2 in the *Reconstituted Opalinus shale* section). The results showed small differences in the void ratios for specimens consolidated at pressures greater than 8 MPa, which implied that the drying shrinkage had less influence on the total volume of highly consolidated and reconstituted specimens. Desbois *et al.* (2009) reported a similar pore morphology or microstructure between frozen and oven-dried samples of the high plasticity Boom clay. Similar observations were made by Houben *et al.* (2014) for Mont Terri Opalinus shale specimens prepared using air drying, oven drying, and freeze drying. In the present study, the oven-drying method was selected to dehydrate both the natural and reconstituted shale specimens for all microstructural experiments. To decrease the desiccation effects of oven drying, the shale specimens were stored in a desiccator that contained a saturated NaCl solution for 24 h and were then air dried for 2 d prior to oven drying at 105ºC for 24 h.

RESULTS AND DISCUSSION

Microfabric and diagenetic properties

The SEM micrographs of a broken surface of a natural Opalinus shale specimen revealed a heterogeneous microfabric with numerous calcareous microfossils and non-clay particles within the folded and warped clay platelets that are prevalent throughout the shale matrix (Figure 4). Amongst the non-clay particles, the framboidal crystals of iron pyrite (Figures 4a, 4b) were easily detected and were dispersed in the shale matrix in the form of either individual or coalesced crystals. The microfossils within Opalinus shale were
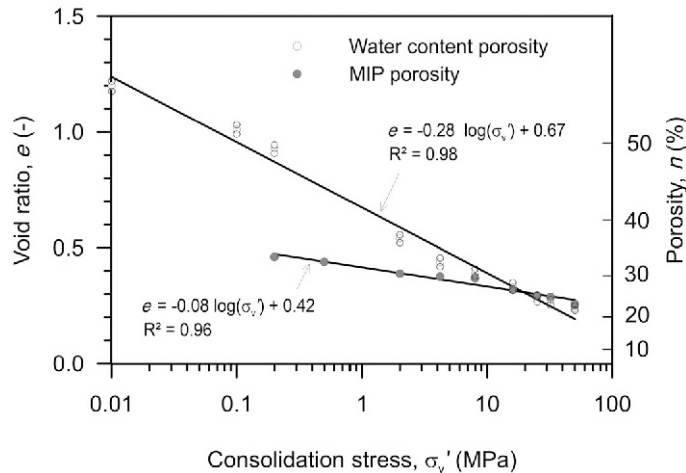
Figure 3. The void ratio of dried reconstituted specimens measured using Hg porosimetry analysis, where the shrinkage after drying was more pronounced for stresses <8 MPa. Note that the marker used for the data covers the error bar (see data in Table 3 and Table 4).

mainly calcareous Foraminifera shells (Figures 4c, 4d). The SEM images of the 2D Ar ion-milled surfaces of the natural shale demonstrate a highly compacted fabric with enhanced pore structures along the boundaries of microfossils and the non-clay particles (Figure 5). The microcracks and fissures form a pore network where the majority of the cracks are randomly distributed along the particle boundaries.

A back-scattered electron micrograph (BSEM) of a broad surface of natural Opalinus shale (Figure 6a) and the fissility plane direction is horizontal. This BSEM photomicrograph provides detailed information on the petrofabrics of Opalinus shale and demonstrates the variability and heterogeneity. The material exhibits a pronounced microfabric that consists of clay aggregates and tabular non-clay particles, which are preferentially oriented parallel to the fissility plane. Inter-aggregate microcracks are abundant and show a similar preferred orientation. The mineral phase distribution determined by EDS was mapped on the same micrograph (Figure 6b). Amongst the different mineral phases in this image, the Ca phase is highlighted (Figure 6c) and is mainly associated with calcite particles and calcareous Foraminifera microfossils. The microfossil shells are dispersed throughout the clay matrix in the form of single 'half-moon' shaped objects, but the other calcite particles are more likely the major source of cementation in the Opalinus shale. The BSEM micrographs can provide evidence of fabric alteration, such as dissolution and transformation of different mineral phases during burial diagenesis. Close up panels within the shale specimen surface (Figure 6a) were selected to explore the evidence for diagenesis (Figure 7). The calcareous microfossils were observed to be locally infilled and rimmed by calcite cement (Figures 7a, 7b). This observation was associated with evidence for the dissolution of early formed calcite cement, which can potentially be replaced by later phases, such as quartz

Table 3. Reconstituted specimens analyzed in the present study under a wide range of effective applied stresses (0.01−50 MPa).

Specimen	Consolidation stress (MPa)	w (%)	e^*	n
Recon.1	0.01	43.55±0.81	1.2±0.02	0.54±0.01
Recon.2	0.1	36.73±072	1.01±0.02	0.50±0.01
Recon.3	0.2	33.64±0.65	0.93±0.02	0.48±0.01
Recon.4	2.0	19.58±0.62	0.54±0.02	0.35±0.01
Recon.5	4.2	15.90±0.68	0.44±0.02	0.30±0.02
Recon.6	8.0	14.30±0.58	0.39±0.02	0.28±0.02
Recon.7	16.0	12.12±0.63	0.33±0.02	0.25±0.02
Recon.8	25.0	10.20±0.52	0.28±0.01	0.22±0.02
Recon.9	32.0	9.62±0.42	0.26±0.01	0.21±0.01
Recon.10	50.0	8.75±0.34	0.24±0.01	0.19±0.01

* Note: $e = wG_s/S_r$ and $n = e/(1+e)$, where w is the water content, G_s is the specific gravity (Table 1), and S_r is the degree of saturation of reconstituted specimens (fully saturated, $S_r = 1.0$).
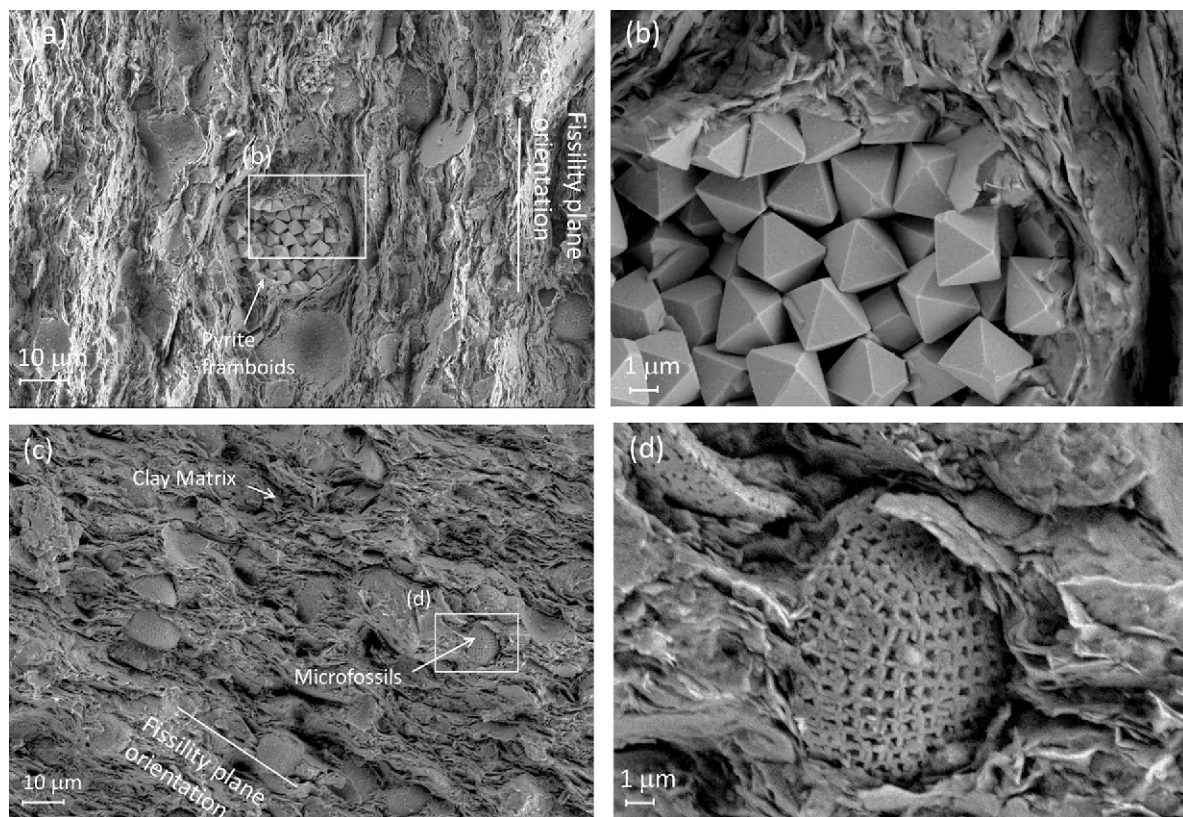
Figure 4. SEM photomicrographs of the broken surface of a natural Opalinus shale specimen with (a, b) pyrite framboids and (c, d) Foraminifera microfossils within the highly oriented clay structure that is parallel to the fissility plane.

and pyrite (*e.g.*, Shaw and Primmer, 1991). The inclusion of pyrite crystals in calcite cement that infills the microfossils and the partial replacement of a calcite particle with anatase are other diagenesis footprints in the Opalinus shale (Figures 7b, 7c, and 7d). The transformation of smectite clay minerals into illites and chlorites (illitization and chloritization) is the most important consequence of deep burial (Potter *et al.*, 2005), which is reflected in the mineralogy of the Opalinus clay (Table 2).

Reconstituted Opalinus shale

The reconstituted specimens were consolidated over a wide range of effective stress levels. The total void ratio (and porosity) of the materials were calculated using the water content data and the specific gravity ($G_s = 2.75$) listed in Table 3. Natural Opalinus shale core specimens with two different fissility formations were compared with a reconstituted shale specimen consolidated along the vertical axis (Figure 8). The image shows fractures, fissility planes, and heterogeneities in the natural specimens, while these features appear to be entirely absent in the reconstituted specimen. The fractures in the natural shale are generally believed to be due to the effects of disturbance, for instance during the unloading and the

release of *in situ* confining stress or due to shrinkage. The consolidation behavior of the reconstituted Opalinus shale and the generic sedimentation curves that were proposed by Skempton (1969) were based on gravitational compression of quaternary argillaceous sediments (Figure 9). The compression behavior of reconstituted Opalinus shale is well described by a linear relation between the void ratio, e, and log σ'_v values and conforms closely to the behavior predicted by Skempton (1969). The maximum burial depth of Opalinus shale is estimated to have been about 1,350 m during the Cretaceous. The maximum effective stress at this depth can be calculated using the following relationship (*e.g.* Budhu, 2000) by assuming that the shale formation is fully saturated:

$$\sigma'_p = \sigma_p - u = (\gamma_{\text{sat}} - \gamma_{\text{w}})h = (1 - n)(G_s - 1)\,\gamma_{\text{w}}h \qquad (2)$$

where, σ'_p is the maximum vertical effective stress, σ_p is the maximum total stress (lithostatic pressure), u is the pore water pressure at depth h, γ_{sat} and γ_w are the unit weights of the saturated sediments and water (9.81 kN/m^3), n is the porosity, G_s is the specific gravity of the shale ($G_s = 2.75$, Table 1), and n is the total porosity. The effective stress at depth h of a saturated soil layer depends on the porosity of the overlaying material. The porosity of the consolidated
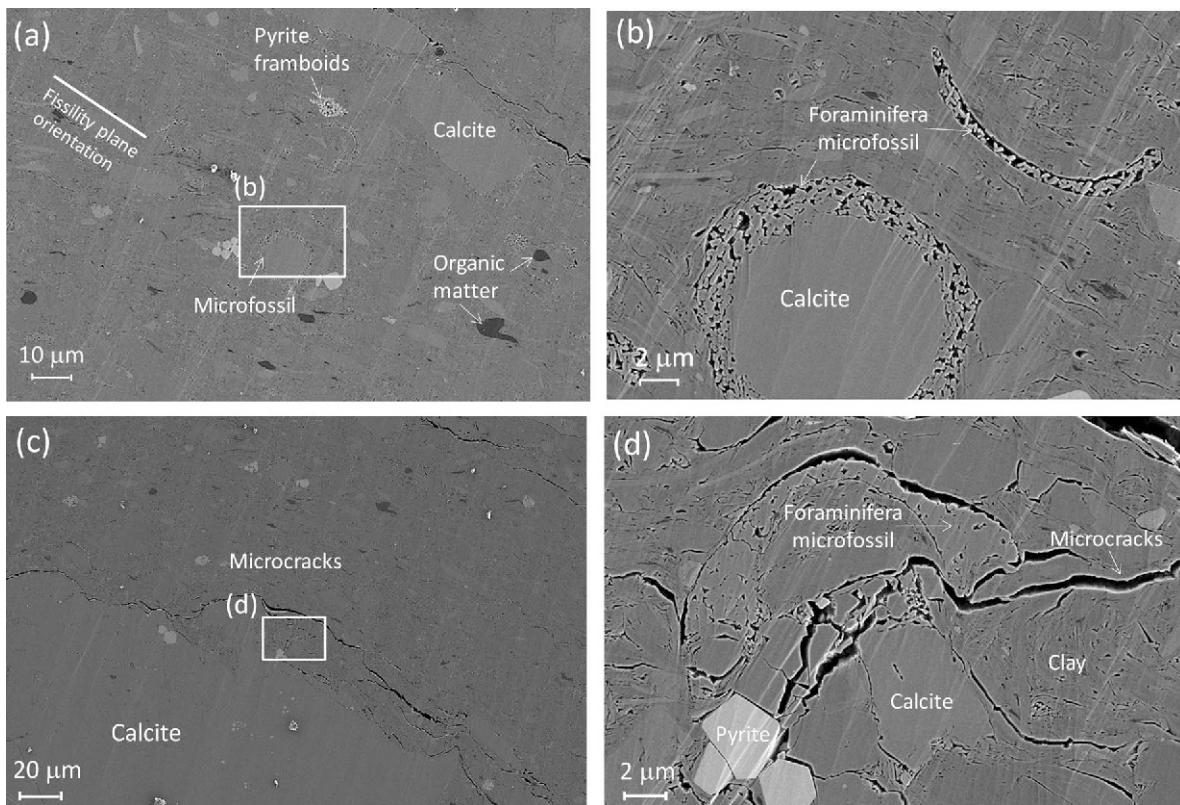
Figure 5. SEM photomicrographs (a, b, c, d) of an Ar ion-milled surface of a natural Opalinus shale specimen. The micron-scale pores resulted from the enhanced porosities along the boundaries of microfossils and non-clay particles or due to the presence of microcracks.

sediments at the end of the primary consolidation during the Cretaceous must have been larger than the current porosity. In order to over-estimate the maximum effective stress, however, a current porosity of $n = 0.17$ was assumed for the natural Opalinus shale. Accordingly, the maximum effective stress at depth $h \sim 1,350$ m calculated using equation 2 resulted in a σ'_p value of ~ 19.2 MPa and the current overburden depth of $h \sim 300$ m resulted in a σ'_v value of ~ 4.3 MPa. The porosity of reconstituted shale that corresponded to these effective stress levels were 0.24 and 0.31, which indicated porosity differences of $\Delta n = 0.07$ and 0.14, respectively, for the maximum depth ($h \sim 1,350$ m) and current depth ($h \sim 300$ m) of the shale formation with an *in situ* porosity of 0.17 (Figure 9). The effective stress to depth conversion was approximated in previous works (*e.g.*, Rossi and Alaminos, 2011) based on the average lithostatic and hydrostatic gradients of 21.6 and 9.8 kPa/m, respectively, which correspond to average bulk and water densities of 2.2 and 1.0 g/cm^3, respectively. Using this conversion, effective stress at the maximum depth ($h \sim 1,350$ m) and current depth ($h \sim 300$ m) of the formation were 15.9 and 3.5 MPa, respectively, which are fairly close to values obtained using equation 2. The overall reduction in void ratio due to creep (Δe_c) can be calculated using the following equation (modified from Mesri, 1973):

$$\Delta e_c = C_\alpha \log\left(\frac{t_{\text{EOP}} + \Delta t}{t_{\text{EOP}}}\right) \quad (3)$$

where, C_α is the material-dependent coefficient of secondary consolidation, t_{EOP} is the *in situ* time at the end of primary consolidation, and Δt is the creep time. According to Mesri (1973), for sedimented (undisturbed) soils, C_α decreases with an increase in the final consolidation pressure. Based on the consolidation results in the present study, the reconstituted shale material was consolidated at a stress level of 32 MPa (Recon.9, specimen height = 12.5 cm) and a coefficient of secondary consolidation value of $C_\alpha \sim 0.01$ was obtained. The time at the end of the primary consolidation was recorded as $t_{\text{EOPL}} = 4.6$ d and the void ratio, e, was 0.26. For a maximum deposition depth of 1,350 m for Opalinus shale, the time at the end of primary consolidation at the site can be estimated using $t_{\text{EOP}} = t_{\text{EOPL}}[(d_F/d_L)^2] \sim 1,470,000$ y by considering a constant coefficient of consolidation, where d_F is the depth of the deposition at the site and d_L is the specimen height in the lab (in this example, $d_L = 0.125$ m; $t_{\text{EOPL}} = 4.6$ d). The change in void ratio due to creep for the 170 Million y can be estimated from equation 3 as $\Delta e_c \sim 0.02$ which resulted in $\Delta n_c = \Delta e_c/(1+e_c)^2 \sim 0.01$, where
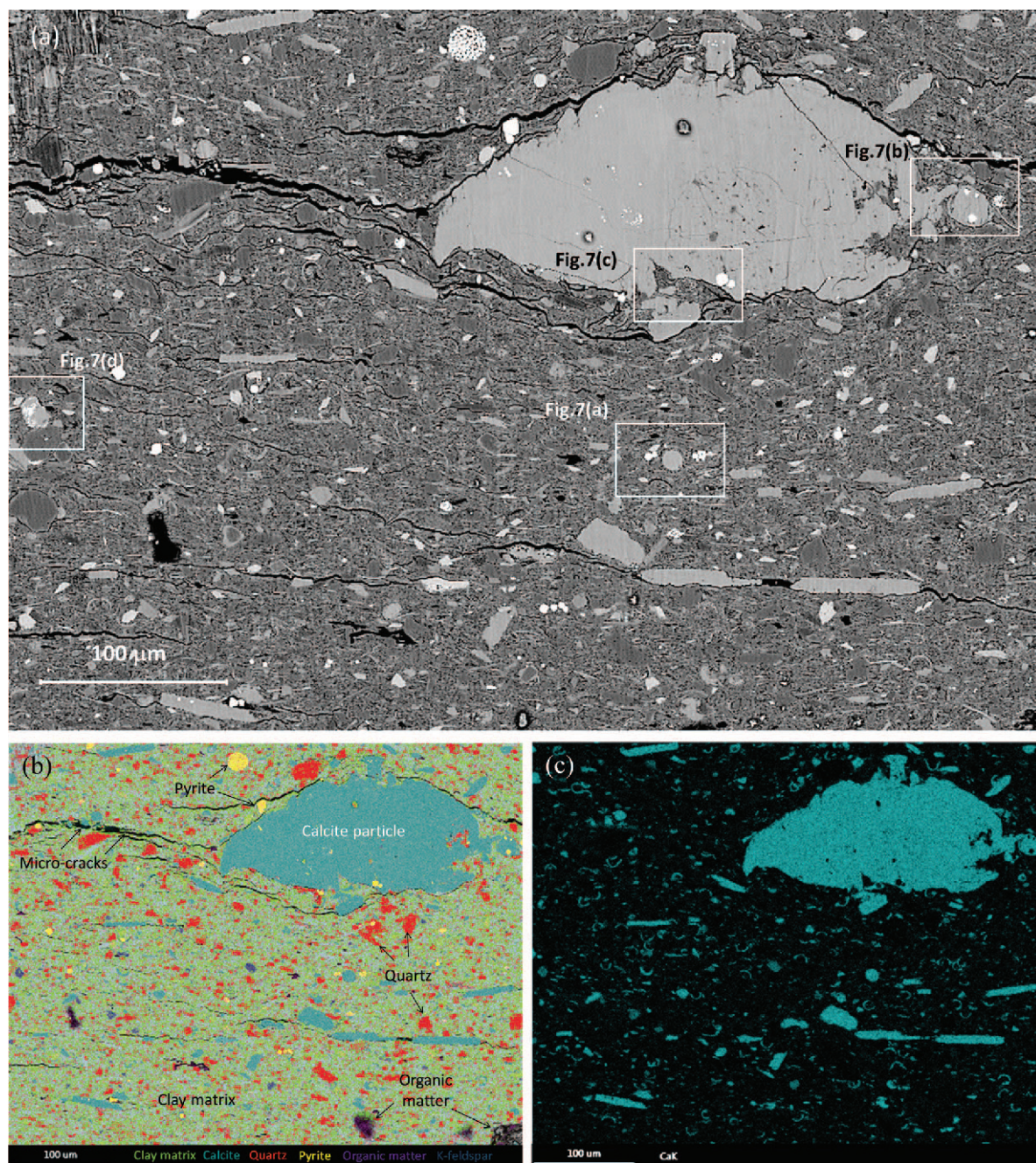
Figure 6. BSE photomicrograph of a broad surface of a natural Opalinus shale sample: (a) the particle orientations and structures can be detected and the horizontal fissility planes and inter-particle cracks are visible, (b) EDS map of the same section provides information on the distribution of mineral phases, and (c) calcium carbonate map of the same section to illustrate the calcareous microfossils and calcite particles.

Δn_c is the change of porosity due to creep. The difference between the porosity of the reconstituted shale and the *in situ* porosity can be determined by taking into account the change due to the creep process and would be estimated as 0.06 or about 35%. Such a discrepancy cannot be explained by gravity driven consolidation and creep processes, but it can be more credibly linked to a re-

precipitation process that caused infilling of the pore space.

Pore structural evolution and diagenesis

Microfabric observation. The BSE photomicrographs of reconstituted shale specimens were collected for samples consolidated at three stress levels ($\sigma'_v = 2$, 16, and
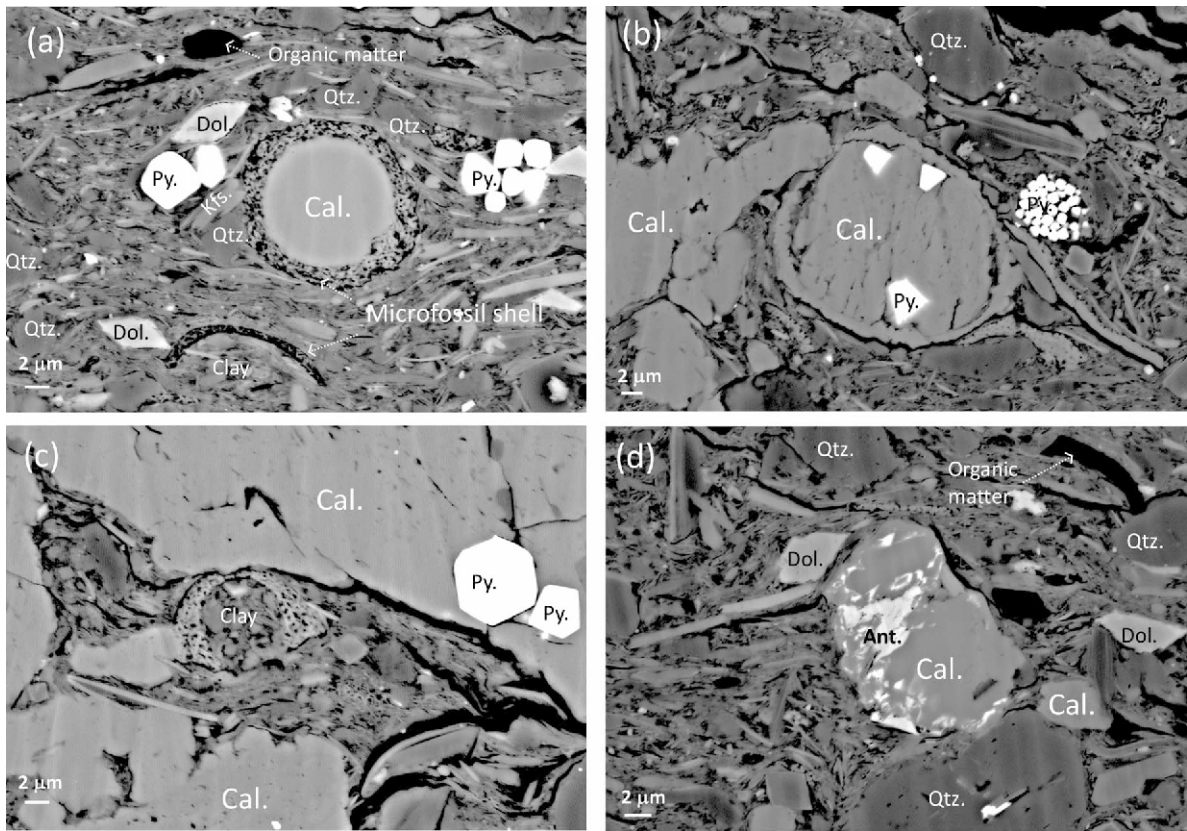
Figure 7. BSE photomicrographs to show: (a) infilling of microfossil shells by calcite (Cal.) and the inclusion of dolomite (Dol.) particles; (b) coalesced and individual pyrite (Py.) framboids within the calcite cement which infills and rims a microfossil shell; (c, d) partial replacement of calcite particles with other minerals.

50 MPa) and two magnifications (Figure 10). At high magnification (Figures 10b, 10d, and 10f), the images show lamellar clay aggregates, which consist of individual particles with a face-to-face association. The non-clay inclusions, which were mainly quartz, calcite, pyrite, and siderite particles appear to be randomly dispersed throughout the structure (Figures 10a, 10c, and 10e). The clay aggregates appear to form face-to-edge and face-to-face contacts with other clay aggregates or with non-clay particles. The dark black colors usually
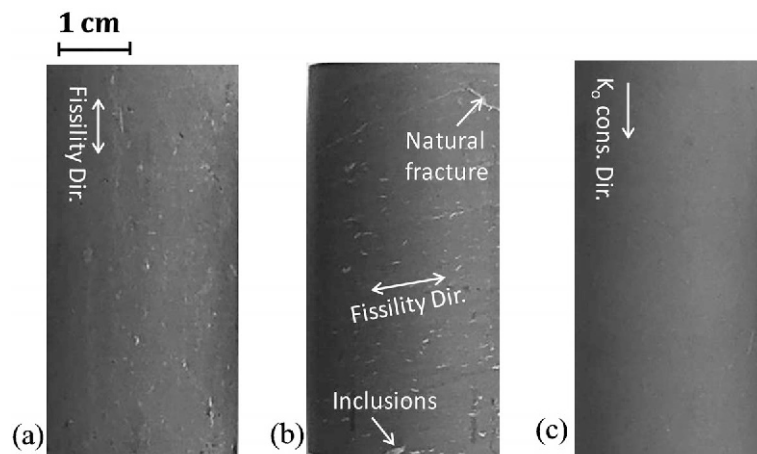

Figure 8. Photographs of (a, b) natural Opalinus shale that show the fissility direction, natural fracture, and non-clay mineral inclusions and (c) photographs of a reconstituted Opalinus shale (Recon.9) consolidated to effective stress of $\sigma'_v = 32$ MPa. The natural variability is evident in the natural material, but has been largely eliminated in the reconstituted shale.
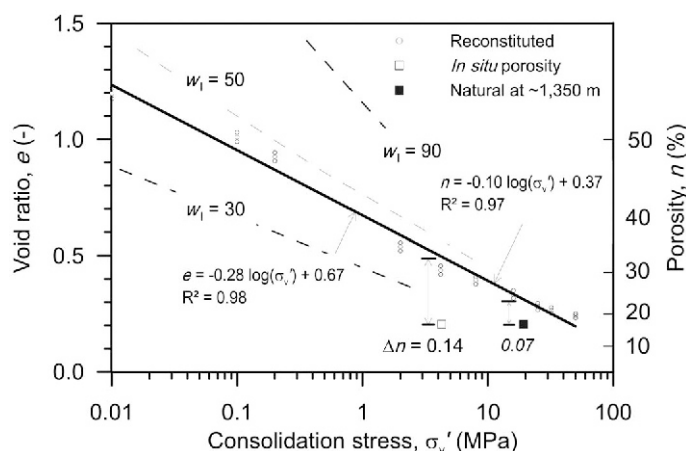
Figure 9. Graph of consolidation stress *vs.* void ratio and porosity of the reconstituted Opalinus shale in the present study along with sedimentation compression curves that were compiled for normally consolidated argillaceous sediments (modified from Skempton, 1969).

indicate the pore space except for the isolated patches of organic matter marked on the images. The pore structure of the reconstituted shales can be partitioned into inter-cluster and intra-cluster pores, where 'cluster' refers to the clay aggregates or non-clay inclusions. Intra-cluster pores include high aspect ratio tabular pores within the clay aggregates, inter-crystalline pores in the pyrite, internal pores in the microfossil shells, and dissolution-rim pores. In contrast, the inter-cluster pores occur between the clay aggregates or the non-clay inclusions with an angular or low aspect ratio and tabular shape. The inter-cluster pores ranged in size from $0.1-1$ μm and showed a significant decrease in size as the level of applied consolidation stress was increased. The inter-cluster pores were almost non-existent for specimens consolidated to 50 MPa (Figures 10e, 10f) with a corresponding total porosity of $n = 0.19$ (Figure 9). Specimens of natural Opalinus shale have an average total porosity of $n = 0.17$, which is relatively close to the Recon.10 specimen and has very similar cluster structures at the same magnifications (Figures 10g, 10h). The natural specimens also showed a prominent network of microcracks that were preferentially oriented towards the horizontal fissility plane, which is a feature not seen in the reconstituted specimens. While the inter-cluster pores showed a clear evolution with the level of consolidation stress, only a small apparent change in the intra-cluster pores was observed. Similar effects have been described in compacted clay specimens (Al-Mukhtar *et al.*, 1996; Simms and Yanful, 2002; Romero and Simms, 2008; Koliji *et al.*, 2010; Seiphoori *et al.*, 2014). The non-clay particles, particularly those developed as the result of diagenesis, such as calcite, ranged in size from $1-10$ μm and are distributed throughout the reconstituted shale specimens. In contrast, much larger calcite particles (up to 100 μm, Figure 6) can be identified in the natural shale. These larger particles appear to have been comminuted during

the grinding process, while cementation bonds, such as carbonate bridges, were also disintegrated. Accordingly, the reconstitution likely removed the main sources of diagenetic bonding. According to Corkum and Martin (2007), the large population of microcracks in natural shale (Figure 10g) can be associated with the breakage of the diagenetic bonds due to tensile strain (*e.g.*, unloading due to the release of *in situ* confining stress) and thus results in the formation and opening of microcracks. This mechanism is explained by the locked-in latent strain energy of the diagenetic bonds described by Bjerrum (1967). Most microcracks are observed to be dispersed throughout the structure with an inter-grain pattern.

Mercury intrusion porosimetry (MIP). The MIP measurement provides direct quantitative information on the evolution of the pore structure of the reconstituted shales at different levels of consolidation stress. Figure 11 summarizes the MIP measurements of the cumulative void ratio, e_{HG} (as well as the cumulative porosity, n_{HG}) *vs.* the pore throat diameter, d, for reconstituted Opalinus shale specimens. Touret *et al.* (1990) suggested that the clay intra-aggregate pores are in the $0.1-0.2$ μm range, while inter-aggregate pores are in the $0.2-3$ μm range. Similarly, Kuila and Prasad (2013) assumed that the intra-aggregate pores of a mixed illite and smectite clay are less than 0.1 μm. In the present study, an equivalent pore diameter of $d = 0.10$ μm was assumed as a partition threshold to distinguish between inter-cluster and intra-cluster pores within the shale material. Using this assumption, the total porosity from MIP analysis (n_{MIP}) was partitioned into inter- (n_1) and intra- (n_2) cluster fractions, such that $n_{MIP} = n_1 + n_2$. The total porosities were calculated by measuring the total volumes of the dehydrated specimens during MIP analysis at low pressure:
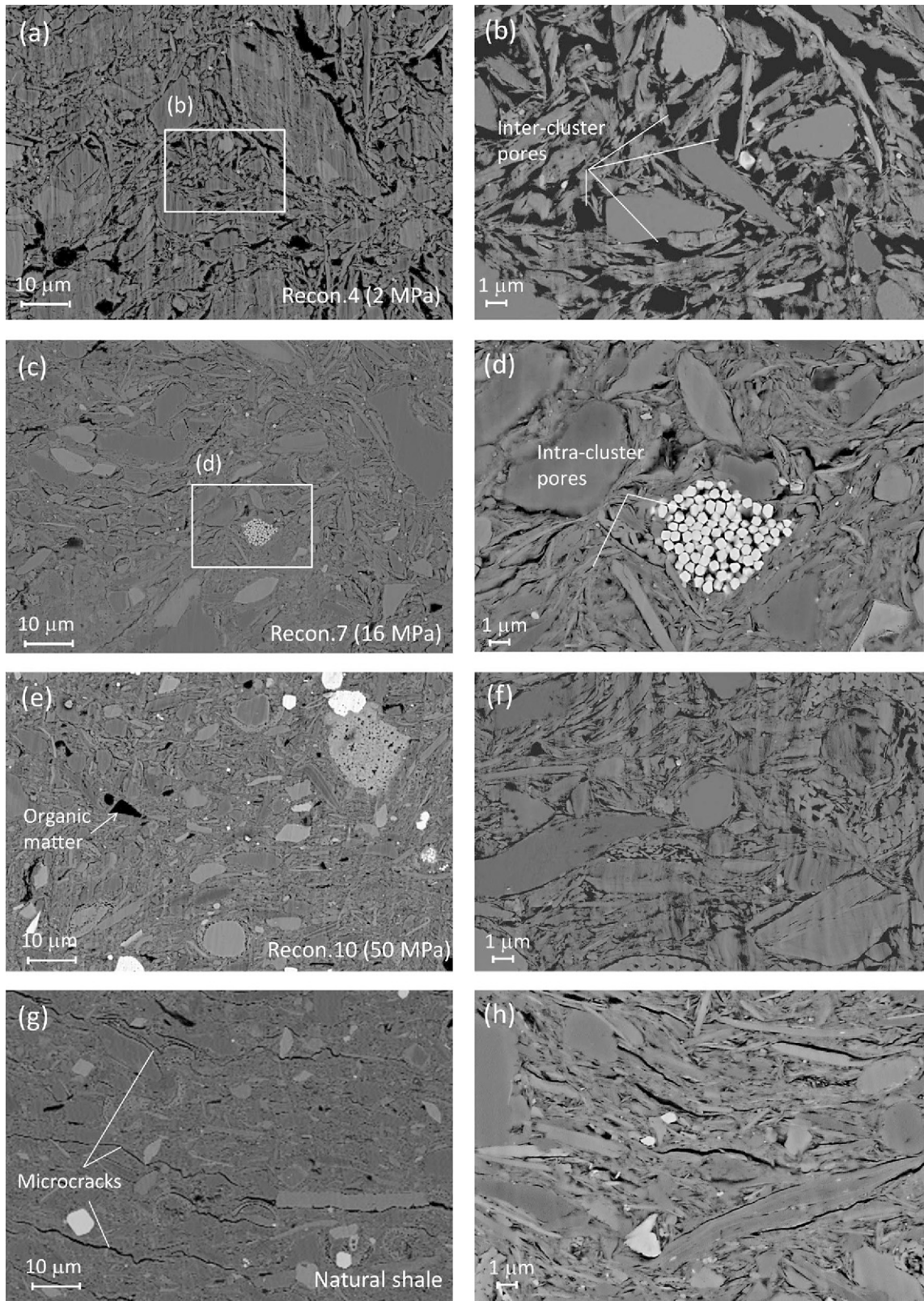
Figure 10. BSE photomicrographs of natural and reconstituted Opalinus shale: (a, b) reconstituted shale at 2 MPa; (c, d) reconstituted shale at 16 MPa; (e, f) reconstituted shale at 50 MPa under one-dimensional K_0-condition; and (g, h) natural shale.
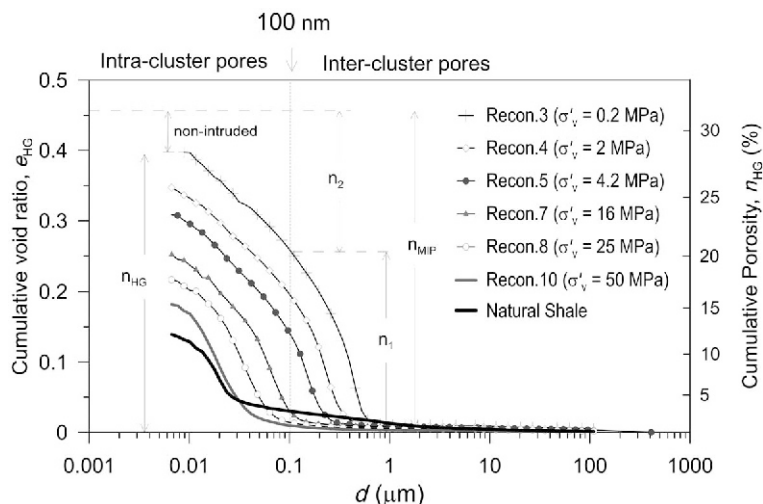
Figure 11. Cumulative void ratios (e_{GH}) of the reconstituted Opalinus shale at different consolidation stress levels and the natural shale.

$$n_{MIP} = \frac{v_V}{V} = \frac{V - V_s}{V} = 1 - \frac{M_s}{G_s g V} \qquad (4)$$

where, V is the total volume of the dehydrated specimen, V_s is the volume of the solid part of the specimen, M_s is the mass of the solid part (*i.e.* the dry mass of the specimen), G_s is the specific gravity of the material (2.75), and g is the acceleration due to gravity (9.81 m/s^2). The inter-cluster porosity (n_1) was obtained from the intruded part of the pore structure for pores greater than 100 nm, as illustrated in Figure 11. The difference between the total porosity from MIP (n_{MIP}) and the intruded porosity (n_{HG}) is due to the existence of non-intruded pores within the material. The intra-cluster porosity (n_2) can, therefore, be calculated from the plot of the cumulative void ratio (Figure 11). The inter-cluster

porosity ratio is defined as n_1/n_{MIP} and the intruded porosity ratio is defined as n_{HG}/n_{MIP} and were plotted *vs.* the consolidation stress σ'_v in Figure 12. The inter-cluster porosity accounted for 62.5% of the total porosity at $\sigma'_v =$ 0.2 MPa, but only 2% of the total porosity at $\sigma'_v =$ 50 MPa, which indicates the dominant role of consolidation stress on this pore fraction (Table 4). Although the natural shale had a lower total porosity, the inter-cluster porosity ratio was much higher than the Recon.10 specimen, which implied the presence of microcracks in the natural shale specimen as observed in Figure 10g.

The total intruded porosity ratio, n_{HG}/n_{MIP}, also decreased with an increase in consolidation stress level due to an increase in the non-intruded intra-cluster pores within the reconstituted specimens; however, the total intruded porosity ratio of the natural shale was less than the reconstituted specimen at the consolidation stress of
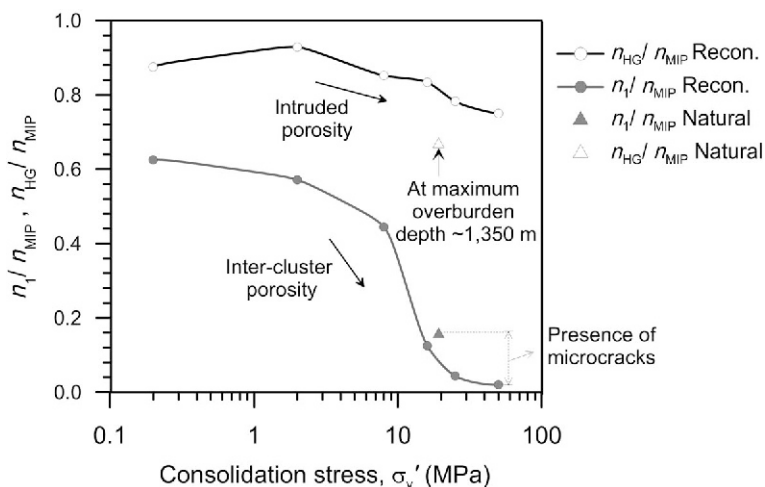

Figure 12. Influence of the applied consolidation stress on the inter-cluster porosity of reconstituted shale material and the measured intra-/inter-cluster porosities for natural shale (note that data markers cover the error bars).

Table 4. Pore structural properties of reconstituted and natural shales obtained from the MIP and nitrogen adsorption/desorption data.

Specimen	Consolidation stress (MPa)	Water content porosity, n^* (−)	MIP total porosity, n_{MIP}^{**} (−)	Inter-cluster porosity ratio, n_1/n_{MIP}	Total intruded porosity ratio, n_{HG}/n_{MIP}	Dominant pore entrance size MIP (nm)	Total pore volume MIP (cm³/g)	BJH Adsorption cumulative volume of pores (cm³/g)	BET surface area (m²/g)	Langmuir surface area (m²/g)	Micropore (external) surface area (m²/g)	BJH adsorption (desorption) average pore diameter (nm)
Recon.3	0.2	0.48	0.32	0.63	0.88	390	0.168	0.067	34	39	4 (30)	10 (9)
Recon.4	2.0	0.35	0.28	0.57	0.93	220	0.141	0.070	36	41	4 (32)	10 (9)
Recon.5	4.2	0.30	0.27	0.41	0.85	150	0.137	0.072	36	41	4 (32)	10 (9)
Recon.7	16	0.25	0.24	0.13	0.83	63	0.116	0.071	37	42	3 (34)	9 (8)
Recon.8	25	0.22	0.23	0.04	0.78	31	0.107	0.070	36	41	2 (34)	10 (9)
Recon.10	50	0.19	0.20	0.02	0.75	18	0.094	0.072	37	42	3 (34)	9 (8)
Natural shale	19.2†	0.17††	0.18	0.16	0.67	18	0.08	0.055	33	37	2 (31)	8 (7)

* n is taken from Table 3.
** n_{MIP} is the porosity of the dehydrated material measured from MIP data presented in Figure 3.
† Based on the maximum effective stress estimated for Opalinus shale.
†† Based on the fluid-displacement technique.

σ'_v = 50 MPa (Table 4). Although the maximum Hg pressure limited the resolution of pores that can be intruded (~7 nm, equation 1), the differences in the total intruded porosity can be attributed to isolated pore structures within the matrix of the natural shale. For instance, the pores within the siderite were apparently poorly interconnected, were not directly connected to the clay matrix (Houben *et al.*, 2013), and, therefore, the complete intrusion of Hg into the pores was not expected. The pore (entrance) size distributions (PSD) for the reconstituted and natural shale specimens were plotted against pore diameter, and the PSD of the natural shale (Figure 13h) exhibited a single dominant equivalent pore diameter of d ~18 nm. The pores within the natural specimen were likely only intra-aggregate/intra-particle pores and the larger pores were associated with the microcracks. In contrast, the PSDs for the reconstituted shales that were consolidated at $\sigma'_v \leqslant 16$ MPa (Figures 13a, 13b, 13c, and 13d) included significant fractions of intra-cluster ($d = 12 - 25$ nm) and inter-cluster pores. The modal value of the inter-cluster pores decreased from 390 nm at $\sigma'_v = 0.2$ MPa to 63 nm at σ'_v = 16 MPa. Further results at higher consolidation pressures showed convergence to a single dominant mode PSD ($d = 31$ nm at $\sigma'_v = 25$ MPa to 18 nm at $\sigma'_v =$ 50 MPa). In this range of stresses, the reconstituted specimens had a broader range of intra-cluster pore sizes than the natural specimen (compare Figures 13f and 13g to Figure 13h). On the other hand, the maximum consolidation stress to form a single dominant equivalent pore size in a reconstituted material is ~2.6 times larger than the estimated maximum effective stress that the Opalinus shale was exposed to during the Cretaceous (see *Reconstituted Opalinus shale* section). This difference reflects the pore structure modifications in natural Opalinus shale that are associated with chemical or chemo-mechanical diagenetic processes.

Nitrogen adsorption experiments. The N$_2$ gas adsorption-desorption isotherms measured for the natural and reconstituted Opalinus shale specimens are presented in Figure 14. All reconstituted samples displayed Type IV isotherms (Schüth *et al.*, 2002; Thommes *et al.*, 2015) typical for monolayer to multilayer adsorption in meso-porous and macroporous solids. The behavior of these samples was very similar in the initial part of the isotherm as well as in the pore condensation branch and was accompanied by H3 type hysteresis. This type of hysteresis loop is commonly observed for microstructures with non-rigid aggregates of plate-like particles (*e.g.* clays) or macropores which are not completely filled with pore condensate (Thommes, 2015). The hysteresis between the adsorption and desorption branches is associated with the presence of mesopores (2−50 nm), while the absence of a plateau at high p/p_0 values indicates macropores (>200 nm). A characteristic 'forced closure' of the desorption branch was observed at $p/p_0 =$
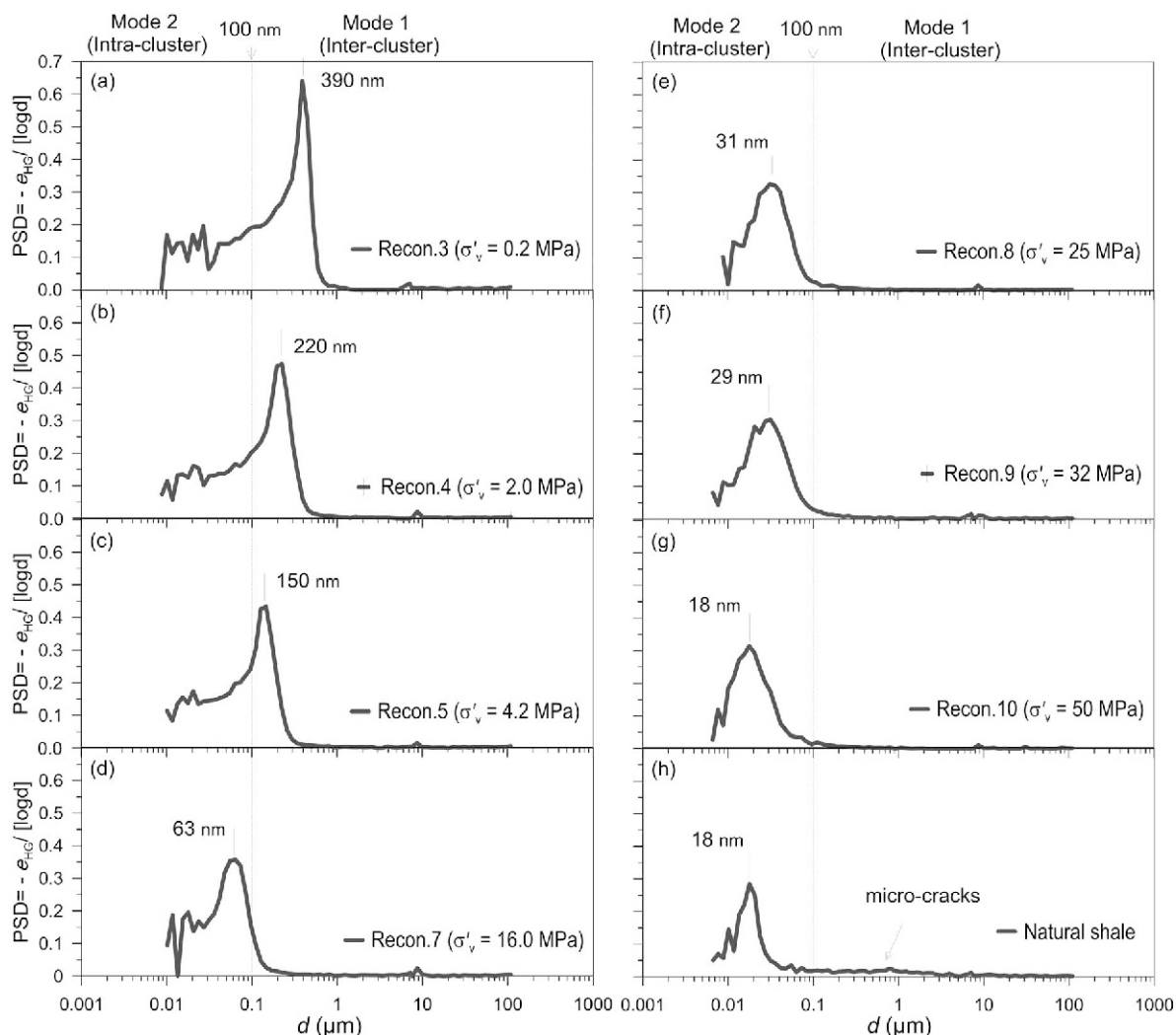
Figure 13. Pore (entrance) size distribution (PSD) functions of reconstituted Opalinus shale samples at different consolidation stress levels and the PSD of the natural shale. A clear transition from a double-structure to a single structure fabric occurred as a result of the increased consolidation stress.

$0.50-0.45$, which indicates a significant fraction of smaller pores (<4 nm). The specific surface areas of the reconstituted shale specimens oscillated around 36 m^2/g for areas calculated using the BET model and 41 m^2/g for areas calculated using the Langmuir model. In contrast, an increase in consolidation pressure tended to slightly reduce the micropore area at the expense of external surface area (Table 4). A Type IV isotherm with an H3 hysteresis loop was also followed by adsorption and desorption to the natural material; however, in this case, a significantly smaller quantity of N$_2$ was adsorbed at p/p_0 ~1 in comparison to the reconstituted specimens. Although MIP measurements showed that the dominant pore throat size of the natural and the highly consolidated reconstituted ($\sigma'_v = 50$ MPa Recon. 10) Opalinus shale specimens were very similar (~18 nm), and the adsorption measurements revealed a 33% difference in the cumula-tive volume of the micropores and mesopores calculated according to the BJH model (Table 4). On the other hand, MIP measurements showed higher accumulated pore volumes for the reconstituted shales at lower pressures (Recon. 3 and Recon.4) where the modal pore size was greater than 200 nm. Such differences resulted from the fundamental assumptions and limitations of both experimental techniques which sample the porosity of porous solids at different length scales (Schüth, 2002). Finally, adsorption measurements showed that the reconstituted specimens had significantly higher specific surface areas (by the BET or Langmuir models) than the natural shale specimen at all levels of consolidation stress (Table 4). This result can be attributed to the precipitation of minerals within the micropores, which is a diagenetic process that was not replicated in the reconstituted materials.
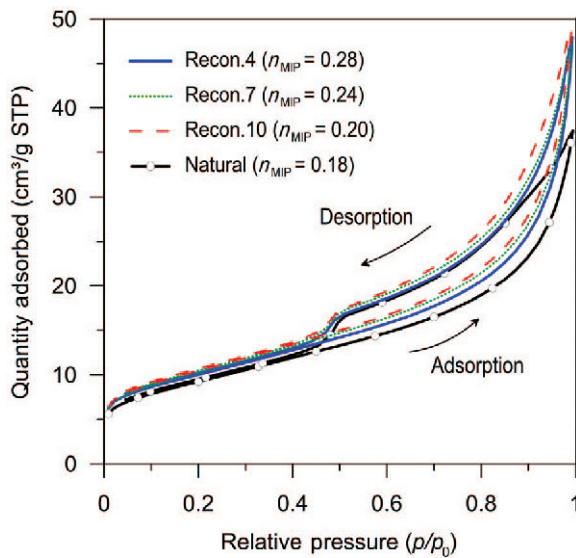
Figure 14. Natural and reconstituted Opalinus shale specimen N_2 adsorption-desorption isotherms at liquid N_2 (-197.3ºC) temperature.

CONCLUSIONS

A new methodology was presented to investigate the effect of diagenetic cementation on the pore structure of natural shale specimens by comparison with reconstituted specimens. The method provided systematic results to follow the evolution of the porosity and pore structure of reconstituted shales under increased effective stresses. The method also gives insight into the role that diagenetic cementation had in reducing the porosity and modifying the pore structure of the natural material.

The reconstituted shale was consolidated under effective stresses comparable to the maximum effective stress that the natural shale has undergone; however, the total porosity obtained by the gravity driven consolidation and creep processes was about 35% larger than the *in situ* porosity of the natural shale. Such a discrepancy can be credibly linked to the diagenetic cementation process that caused infilling of pore space and reduced the total porosity.

The Hg intrusion porosimetry measurements revealed a progressive size reduction in the dominant entrance pores of the reconstituted shale specimens due to an increase in the consolidation stress, while a clear transition from a double-structured microfabric to a single-structured microfabric was observed. The maximum consolidation stress to form a single-structured reconstituted material was 2.6 times larger than the estimated maximum effective stress that the Opalinus shale has undergone.

In comparison to reconstituted shale specimens at higher effective stresses, the natural shale samples had lower adsorbed N_2 volumes, specific surface areas, and total porosities. Moreover, the combined Hg intrusion porosimetry and N_2 gas adsorption approaches revealed significant changes in the reconstituted specimen mesostructures, but consolidation stresses only had a minor impact on nano-level fabric. This observation suggests that time dependent chemo-mechanical diagenetic processes affected the natural shale, which could not be reproduced in consolidation experiments on the reconstituted shale specimens.

NOTATION

d = pore entrance diameter
d_F = the depth of deposition at the site
d_L = the specimen height in the lab
Δt = the creep time
C_α = the coefficient of secondary consolidation
e = the void ratio
e_{HG} = the cumulative intruded void ratio
G_s = the specific gravity
γ_{Hg} = the surface tension of Hg
M_s = the solid mass of the specimen
n = the total porosity
n_1 = the inter-cluster porosity
n_2 = the intra-cluster porosity
n_{HG} = the intruded porosity calculated from MIP
n_{MIP} = the total porosity calculated from MIP
K_0 = the static lateral pressure coefficient
p_{Hg} = the mercury pressure
p = the absolute equilibrium pressure of N_2
p_0 = the condensation pressure of N_2
PSD = the pore size density function
RH = the relative humidity
ρ_h = the density at hygroscopic condition
S_r = the degree of saturation of specimen
σ'_p = the maximum vertical effective stress
σ'_v = the vertical effective stress, consolidation stress
T = the temperature
t_{EOP} = the time at the end of the primary consolidation
θ = the contact angle between Hg and the soil particles
V = the total volume of the specimen
V_s = the solid volume of the specimen
w_L = the liquid limit
w_P = the plastic limit

REFERENCES

Abdulhadi, N.O., Germaine, J.T., and Whittle, A.J. (2010) Experimental study of wellbore instability in clays. *Journal of Geotechnical and Geoenvironmental Engineering*, **137**, 766−776.

Adams, A.L., Germaine, J.T., Flemings, P.B., and DayStirrat, R.J. (2013) Stress induced permeability anisotropy of oriented Boston Blue Clay. *Water Resources Research*, **49**, 6561−6571.

Allman, M. and Atkinson, J. (1992) Mechanical properties of reconstituted Bothkennar soil. *Géotechnique*, **42**, 289−301.

Al-Mukhtar, M., Belanteur, N., Tessier, D., and Vanapalli, S. (1996) The fabric of a clay soil under controlled mechanical and hydraulic stress states. *Applied Clay Science*, **11**, 99−115.

Ambrose, R.J., Haryman, R.C., Diaz-Campos, M., Akkutlu, I.Y., and Sondergeld, C.H. (2012) Shale gas in-place calculations part 1: New pore-scale considerations. *SPE Journal*, **17**, 219−229.

Awwiller, D. (1993) Illite/smectite formation and potassium mass transfer during burial diagenesis of mudrocks; a study from the Texas Gulf Coast Paleocene-Eocene. *Journal of Sedimentary Research*, **63**, 501−512.

Barrett, E.P., Joyner, L.G., and Halenda, P.P. (1951) The determination of pore volume and area distributions in porous substances: I. Computations from nitrogen isotherms. *Journal of the American Chemical Society*, **723**, 373−380.

Bjerrum, L. (1967) Progressive failure in slopes of over-consolidated plastic clay and clay shales: Third Terzaghi Lecture. *Journal of Soil Mechanics and Foundations Division*, **93**, 1−49.

Bjørlykke, K. and Aagaard, P. (1992) Clay minerals in North Sea sandstones. Pp. 65−80. In Houseknecht, D.W. and Pittman, E.D. (eds) *Origin, Diagenesis, and Petrophysics of Clay Minerals in Sandstones*. SEPM Special Publication, **47**.

Bock, H. (2000) RA Experiment: Data report on rock mechanics - Mont Terri project. *NAGRA Technical Report TN00-02*, Q+S Consult, Germany.

Brunauer, S., Emmett, P.H., and Teller, E. (1938) Adsorption of gases in multimolecular layers. *Journal of the American Chemical Society*, **60**, 309−319.

Budhu, M. (2000) *Soil Mechanics and Foundations*. John Wiley and Sons, Inc., New York.

Burland, J. (1990) On the compressibility and shear strength of natural clays. *Géotechnique*, **40**, 329−378.

Burton, G.J., Pineda, J.A., Sheng, D., and Airey, D. (2015) Microstructural changes of an undisturbed, reconstituted and compacted high plasticity clay subjected to wetting and drying. *Engineering Geology*, **193**, 363−373.

Chalmers, G.R. and Bustin, R.M. (2015) Porosity and pore size distribution of deeply-buried fine-grained rocks: Influence of diagenetic and metamorphic processes on shale reservoir quality and exploration. *Journal of Unconventional Oil and Gas Resources*, **12**, 134−142.

Chandler, R. J. (2010) Stiff sedimentary clays: geological origins and engineering properties. *Géotechnique*, **60**, 891-902.

Clarkson, C.R., Wood, J., Burgis, S.E., Aquino, S.D., Freeman, M., and Birss, V.I. (2012) Nanopore structure analysis and permeability predictions for a tight gas/shale reservoir using low-pressure adsorption and mercury intrusion techniques. *Proceedings SPE Americas Unconventional Resources Conference 2012*, Society of Petroleum Engineers.

Corkum, A.G. and Martin, C.D. (2007) The mechanical behaviour of weak mudstone (Opalinus Clay) at low stresses. *International Journal of Rock Mechanics and Mining Sciences*, **44**, 196−209.

Cotecchia, F. and Chandler, R.J. (1997) The influence of structure on the pre-failure behaviour of a natural clay. *Géotechnique*, **47**, 523−544.

Cruz, M.R. and Reyes, E. (1998) Kaolinite and dickite formation during shale diagenesis: Isotopic data. *Applied Geochemistry*, **13**, 95−104.

Curtis, C. (1980) Diagenetic alteration in black shales. *Journal of the Geological Society*, **137**, 189−194.

Das, B.M. (2008) *Advanced Soil Mechanics*, 3rd Edition, pp. 25−27. Taylor & Francis, New York.

Desbois, G., Urai, J.L., Kukla, P.A. (2009) Morphology of the pore space in claystones − evidence from BIB/FIB ion beam sectioning and cryo-SEM observations. *eEarth*, **4**, 15−22.

Desbois, G., Urai, J.L., Hemes, S., Brassinnes, S., De Craen, M., and Sillen, X. (2014) Nanometer-scale pore fluid distribution and drying damage in preserved clay cores from Belgian clay formations inferred by BIB-cryo-SEM. *Engineering Geology*, **179**, 117−131.

Desbois, G., Urai, J.L., Kukla, P.A., Konstanty, J., and Baerle, C. (2011) High-resolution 3D fabric and porosity model in a tight gas sandstone reservoir: a new approach to investigate microstructures from mm- to nm-scale combining argon beam cross-sectioning and SEM imaging. *Journal of Petroleum Science and Engineering*, **78**, 243−257.

Diamond, S. (1970) Pore size distributions in clays. *Clays and Clay Minerals*, **18**, 7−23.

Dræge, A., Jakobsen, M., and Johansen, T.A. (2006) Rock physics modelling of shale diagenesis. *Petroleum Geoscience*, **12**, 49−57.

Dullien, F.A. (1975) New network permeability model of porous media. *AIChE Journal*, **21**, 299−307.

Favero, V., Ferrari, A., and Laloui, L. (2016) On the hydro-mechanical behaviour of remoulded and natural Opalinus Clay shale. *Engineering Geology* **208**, 128−135.

Freivogel, M. and Huggenberger, P. (2003) Modellierung bilanzierter profile im gebiet Mont Terri−La Croix (Kanton Jura): Mont Terri Project−Geology, paleohydrogeology and stress field of the Mont Terri region. *Federal Office for Water and Geology Rep*, **4**, 7−44.

Gaupp, R., Matter, A., Platt, J., Ramseyer, K., and Walzebuck, J. (1993) Diagenesis and fluid evolution of deeply buried Permian (Rotliegende) gas reservoirs, northwest Germany. *AAPG Bulletin*, **77**, 1111−1128.

Germaine, J.T. (1982) *Development of the Directional Shear Cell for Measuring Cross Anisotropic Clay Properties*. PhD Thesis, Dept. Civil & Environmental Engineering, MIT, Cambridge, MA.

Gregg, S.J. and Sing, K.S.W. (1983) *Adsorption, Surface Area, and Porosity* (2nd edition). Academic Press, New York, Academic Press.

Hillier, S. (1993) Origin, diagenesis, and mineralogy of chlorite minerals in Devonian lacustrine mudrocks, Orcadian Basin, Scotland. *Clays and Clay Minerals*, **41**, 240−240.

Hong, Z.-S., Yin, J., and Cui, Y.-J. (2010) Compression behaviour of remoulded soils at high initial water contents. *Géotechnique* **60**, 691−700.

Houben, M.E., Desbois, G., and Urai, J.L. (2014) A comparative study of representative 2D microstructures in shaly and sandy facies of Opalinus Clay (Mont Terri, Switzerland) inferred form BIB-SEM and MIP methods. *Marine and Petroleum Geology*, **19**, 143−161.

Houben, M., Desbois, G., and Urai, J. (2013) Pore morphology and distribution in the shaly facies of Opalinus Clay (Mont Terri, Switzerland): Insights from representative 2D BIB−SEM investigations on mm to nm scale. *Applied Clay Science*, **71**, 82−97.

Howard, J.J. (1991) Porosimetry measurement of shale fabric and its relationship to illite/smectite diagenesis. *Clays and Clay Minerals*, **39**, 355−361.

Huggett, J.M. (1993) Diagenesis of mudrocks and concretions from the London Clay formation in the London Basin. *Clay Minerals*, **29**, 693−707.

Kim, J-W., Bryant, W., Watkins, J., and Tieh, T. (1998) Electron microscopic observations of shale diagenesis, offshore Louisiana, USA, Gulf of Mexico. *Geo-Marine Letters*, **18**, 234−240.

Koliji, A., Vulliet, L., and Laloui, L. (2010) Structural characterization of unsaturated aggregated soil. *Canadian Geotechnical Journal*, **47**, 297−311.

Kuila, U. and Prasad, M. (2013) Specific surface area and poresize distribution in clays and shales. *Geophysical Prospecting*, **61**, 341−362.

Larson, R., and Morrow, N. (1981) Effects of sample size on capillary pressures in porous media. *Powder Technology*, **30**, 123−138.

Laurich, B., Urai, J.L., Desbois, G., Klaver, J., Vollmer, C., and Nussbaum, C. (2017). Lessons learned from electron microscopy of deformed Opalinus clay. *Advances in Laboratory Testing and Modelling of Soils and Shales*, Springer Series in Geomechanics and Geoengineering. Springer, Cham, p 345−350.

Leroueil, S., Vaughan, P. (1990) The general and congruent effects of structure in natural soils and weak rocks. *Géotechnique*, **40**, 467−488.

Loucks, R.G., Reed, R.M., Ruppel, S.C., and Jarvie, D.M. (2009) Morphology, genesis, and distribution of nanometer-scale pores in siliceous mudstones of the Mississippian Barnett Shale. *Journal of Sedimentary Research*, **79**, 848−861.

Marschall, P., Horseman, S., and Gimmi, T. (2005) Characterisation of gas transport properties of the Opalinus Clay, a potential host rock formation for radioactive waste disposal. *Oil and Gas Science and Technology*, **60**, 121−139.

Mazurek, M., Hurford, A.J., and Leu, W. (2006). Unravelling the multistage burial history of the Swiss Molasse Basin: Integration of apatite fission track, vitrinite reflectance and biomarker isomerisation analysis. *Basin Research*, **18**, 27−50.

Mesri, G. (1973) Coefficient of secondary compression. *Journal of Soil Mechanics and Foundations Division*, ASCE, **99**, pp. 123−137.

Morgan, S.P. (2015) *An Experimental and Numerical Study on the Fracturing Processes in Opalinus Shale*. PhD Thesis, Dept. Civil and Environmental Engineering, MIT, Cambridge, Massachussets, USA.

Ninjgarav, E., Chung, S-G., Jang, W-Y., and Ryu, C-K. (2007) Pore size distribution of Pusan clay measured by mercury intrusion porosimetry. *KSCE Journal of Civil Engineering*, **11**, 133−139.

Nygård, R., Gutierrez, M., Gautam, R., and Høeg, K. (2004) Compaction behavior of argillaceous sediments as function of diagenesis. *Marine and Petroleum Geology*, **21**, 349−362.

Ortega, J.A., Ulm, F.J., and Abousleiman, Y. (2011). The nanogranular origin of friction and cohesion in shale - A strength homogenization approach to interpretation of nanoindentation results. *International Journal of Numerical and Analytical Methods in Geomechanics*, **35**, 1854−1876.

Parker, S. P. (1997) *McGraw-Hill Dictionary of Geology and Mineralogy*, McGraw-Hill Companies.

Péron, H., Laloui, L., and Hueckel, T. (2006) An improved volume measurement for determining soil water retention curves. *Geotechnical Testing Journal*, **30**, 1−8.

Potter, P.E., Maynard, J.B., and Depetris, P.J. (2005) *Mud and Mudstones: Introduction and Overview*. Springer Science & Business Media.

Romero, E. and Simms, P.H. (2008). Microstructure investigation in unsaturated soils: A review with special attention to contribution of mercury intrusion porosimetry and environmental scanning electron microscopy. *Geotechnical and Geological Engineering*, **26**, 705−727.

Rossi, C. and Alaminos, A. (2014). Evaluating the mechanical compaction of quartzarenites: The importance of sorting (Llanos foreland basin, Colombia). *Marine and Petroleum Geology*, **56**, 222−238.

Rutqvist, J. (2012) The geomechanics of CO_2 storage in deep sedimentary formations. *Geotechnical and Geological Engineering*, **30**, 525−551.

Sasanian, S. and Newson, T. (2013) Use of mercury intrusion porosimetry for microstructural investigation of reconstituted clays at high water contents. *Engineering Geology*, **158**, 15−22.

Schneider, J., Flemings, P.B., Day-Stirrat, R.J., and Germaine, J.T. (2011) Insights into pore-scale controls on mudstone permeability through resedimentation experiments. *Geology*, **39**, 1011−1014.

Schüth F., Sing K.S.W., and Weitkamp J. (2002) *Handbook of Porous Solids, Volume 1.* Wiley − VCH, Weinheim.

Scotchman, I. (1989) Diagenesis of the Kimmeridge clay formation, onshore UK. *Journal of the Geological Society*, **146**, 285−310.

Seiphoori, A. (2014) *Thermo-hydro-mechanical Characterisation and Modelling of MX-80 Granular Bentonite*. Ecole Polytechnique Fédérale deLausanne, Lausanne, Switzerland, 10.5075/epfl-thesis-6159.

Seiphoori, A., Ferrari, A., and Laloui, L. (2014) Water retention behaviour and microstructural evolution of MX-80 bentonite during wetting and drying cycles. *Géotechnique*, **64**, 721−734.

Seiphoori, A., Moradian, Z., Whittle, A.J., and Einstein, H.H. (2016) Microstructural Characterization of Opalinus Shale. *50th US Rock Mechanics/Geomechanics Symposium*, the American Rock Mechanics Association.

Shaw, H. and Primmer, T. (1991) Diagenesis of mudrocks from the Kimmeridge clay formation of the Brae area, UK North Sea. *Marine and Petroleum Geology*, **8**, 270−277.

Sheldon, H.A.,Wheeler, J.,Worden, R.H., and Cheadle, M.J. (2003) An analysis of the roles of stress, temperature, and pH in chemical compaction of sandstones. *Journal of Sediment Research*. **73**, 64−71.

Simms, P. and Yanful, E. (2002) Predicting soilùwater characteristic curves of compacted plastic soils from measured pore size distributions. *Géotechnique*, **52**, 269−278.

Skempton, A.W. (1953) The Colloidal Activity of Clay. *Proc. 3rd International Conference on Soil Mechanics and Foundation Engineering*, **1**, 57−61.

Skempton, A.W. (1969) The consolidation of clays by gravitational compaction. *Quarterly Journal of the Geological Society*, **125**, 373−411.

Skempton, A.W. and Jones, O. (1944) Notes on the compressibility of clays. *Quarterly Journal of the Geological Society*, **100**, 119−135.

Slatt, R.M. and O'Brien, N.R. (2011) Pore types in the Barnett and Woodford gas shales: Contribution to understanding gas storage and migration pathways in fine-grained rocks. *AAPG bulletin*, **95**, 2017−2030.

Snyder, R.L. (1992). The use of reference intensity ratios in X-ray quantitative analysis. *Powder Diffraction*, **7**, 186−193.

Thommes M., Kaneko K., Neimark A.V., Oliver J.P., Rodriguez-Reinoso F., Rouquerol J., and Sing K.S.W. (2015) Physisorption of gases, with special reference to the evaluation of surface area and pore size distribution (IUPAC Technical Report). *Pure and Applied Chemistry*, **87**, 1051−1069.

Thompson, M.L., McBride, J.F., and Horton, R. (1985) Effects of drying treatments on porosity of soil materials. *Soil Science Society of America Journal*, **49**, 1360−1364.

Touret, O., Pons, C.H., Tessier, D., and Tardy, Y. (1990) Etude de la répartition de l'eau dans des argiles saturées Mg^{2+} aux fortes teneurs en eau. *Clay Minerals*, **25**, 217−223.

Tourtelot, H.A. (1979) Black shale − its deposition and diagenesis. *Clays and Clay Minerals*, **27**, 313−321.

Washburn, E.W. (1921) The dynamics of capillary flow. *Physical Review*, **17**, 273−283.

Webb, P.A. and Orr, C. (1997) *Analytical Methods in Fine Particle Technology*. Micromeritics, Norcross, Georgia, USA.

William, E. and Airey, D. (2009) The role of fabric in evaluating the failure mode of the stiffened Bringelly Shale. *10th IAEG International Congress. IAEG 2006*. Geological Society of London, United Kingdom, Engineering Geology Special Publications, **22** [on CD-ROM insert, Paper 221].

Yu, C.Y., Chow, J.K., and Wang, Y-H. (2016) Pore size changes and responses of kaolinite with different structures subject to consolidation and shearing. *Engineering Geology*, **202**, 22−131.